SCIENTIFIC REP🐾RTS

OPEN

Soot Combustion over Nanostructured Ceria with Different Morphologies

Wen Zhang, Xiaoyu Niu, Liqiang Chen, Fulong Yuan & Yujun Zhu

In this study, nano-structure ceria with three different morphologies (nanorod, nanoparticle and flake) have been prepared by hydrothermal and solvothermal methods. The ceria samples were deeply characterized by XRD, SEM, TEM, H_2-TPR, XPS and *in-situ* DRIFTS, and tested for soot combustion in absence/presence NO atmospheres under loose and tight contact conditions. The prepared ceria samples exhibit excellent catalytic activities, especially, the CeO_2 with nanorod (Ce-R) shows the best catalytic activity, for which the peak temperature of soot combustion (T_m) is about 500 and 368 °C in loose and tight contact conditions, respectively. The catalytic activity for Ce-R is higher than that of the reported CeO_2 catalysts and reaches a level that of precious metals. The characterization results reveal that the maximal amounts of adsorbed oxygen species on the surface of the nanostructure Ce-R catalyst should be the crucial role to decide the catalytic soot performance. High BET surface area may also be a positive effect on soot oxidation activity under loose contact conditions.

Diesel engines are of great significance to modern society due to their optimal fuel efficiency, low emission of CO_2 and high durability. They are widely used to vehicles, ships and working machines, however, emission of particulate matter (PM) and nitrogen oxides (NO_x) in the process of combustion has been received attention due to causing massive problems to the environment and health, one of them is carbonaceous soot as a major pollutant[1–3]. Therefore, that calls for efficient exhaust gas treatment systems to reduce soot.

The catalytic soot oxidation is one of the most efficient techniques to reduce emission of soot particles. Several kinds of catalysts have exhibited good catalytic performances for diesel soot combustion, such as mixed metal oxides combined with noble metals[3–6], alkaline metal oxides[7,8], transition metal oxides[9–11], perovskite-like type oxides[12–14] and ceria-based oxides[1,15–23]. Among these catalysts, precious metals have good catalytic activity, but they are most expensive. Zhao *et al.* have carried out many valuable researches on the removal of soot[4,6,21,23–25]. A series of three dimensionally ordered macroporous (3DOM) catalysts (Pt/TMO, 3DOM Pt/Fe_2O_3 and Pt/Co_3O_4) were prepared and exhibited much higher catalytic activity for diesel soot combustion in contrast to other catalysts. In addition, CeO_2 has the excellent redox properties, oxygen storages and release capability by the way of facile cycle conversion between Ce^{3+} and Ce^{4+} oxidation states[1,26–29]. Particularly, inserting transition metals into a CeO_2 framework can increase CeO_2 thermal stability and the number of defects which improve its redox properties. CeO_2 doped with transition metals is considered as a good cheap substitute for noble metals catalyst for soot oxidation.

In recent years, numerous studies have shown that CeO_2 with shapes has a positively effect on catalytic performances such as photocatalytic and hydrogen electro-oxidation[30–32]. In this context, CeO_2 could also act as a catalyst in soot oxidation reactions and its physicochemical properties can be influenced by their structural properties[32,33]. Therefore, it is meaningful to prepare CeO_2 catalysts with different shapes and morphologies for investigating their catalytic performances of soot combustion because the activity can be correlated to the exposure of reactive crystal planes and active species in different shapes CeO_2 nanoparticles[32,34–40]. Recently, Trovarelli *et al.*[37] synthesized two types of shape-controlled CeO_2 (nanocubes and nanorods) and compared their catalytic performance for soot combustion. In addition, different morphologies influenced the structure defects of ceria. Bensaid *et al.*[38] reported a hydrothermal method to synthesize CeO_2 with self-assembled stars morphologies, which had high specific surface area (105 m^2/g) and improved the soot-catalyst contact to enhance the activity of

Key Laboratory of Functional Inorganic Material Chemistry (Heilongjiang University), Ministry of Education, School of Chemistry and Materials, Heilongjiang University, Harbin, 150080 P. R. China. Correspondence and requests for materials should be addressed to F.Y. (email: fulongyuan2000@yahoo.com) or Y.Z. (email: yujunzhu@hlju.edu.cn)
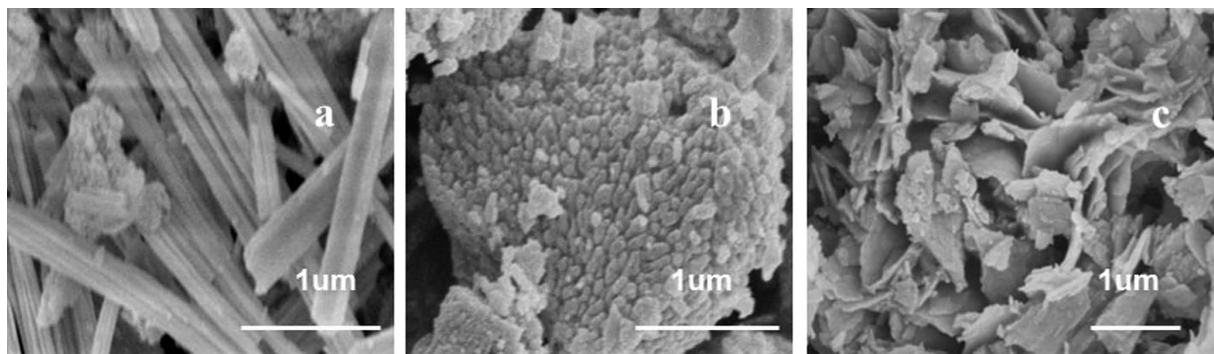
Figure 1. SEM images of (**a**) Ce-R, (**b**) Ce-P and (**c**) Ce-F.
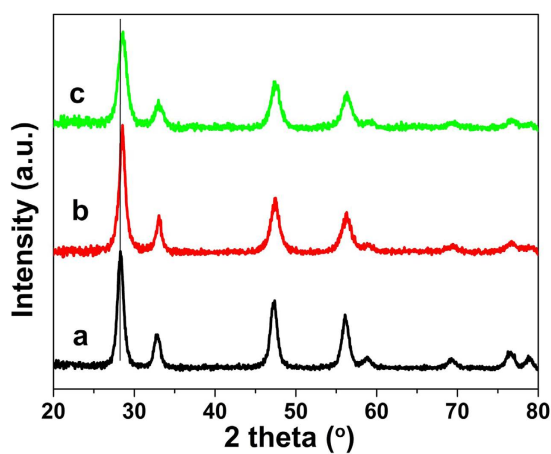
Figure 2. XRD patterns of (**a**) Ce-R, (**b**) Ce-P and (**c**) Ce-F.

soot combustion. Thus, it is meaningful to prepare different morphology of CeO_2 in order to improve its catalytic performance by controlling its surface structure.

Based the effect of shapes on surface physicochemical properties, our present study aims are preparation of CeO_2 with different morphologies and investigation on the relation between the catalytic performance for soot combustion and the shapes. In this work, CeO_2 with three kinds of morphologies including nanorod, nanoparticle and nanoflake were synthesized and justified their catalytic behavior for soot oxidation under different contact conditions in absence/presence NO atmospheres. The CeO_2 with nanorod exhibited the best catalytic activity, and it reached a level that of a precious metal catalyst.
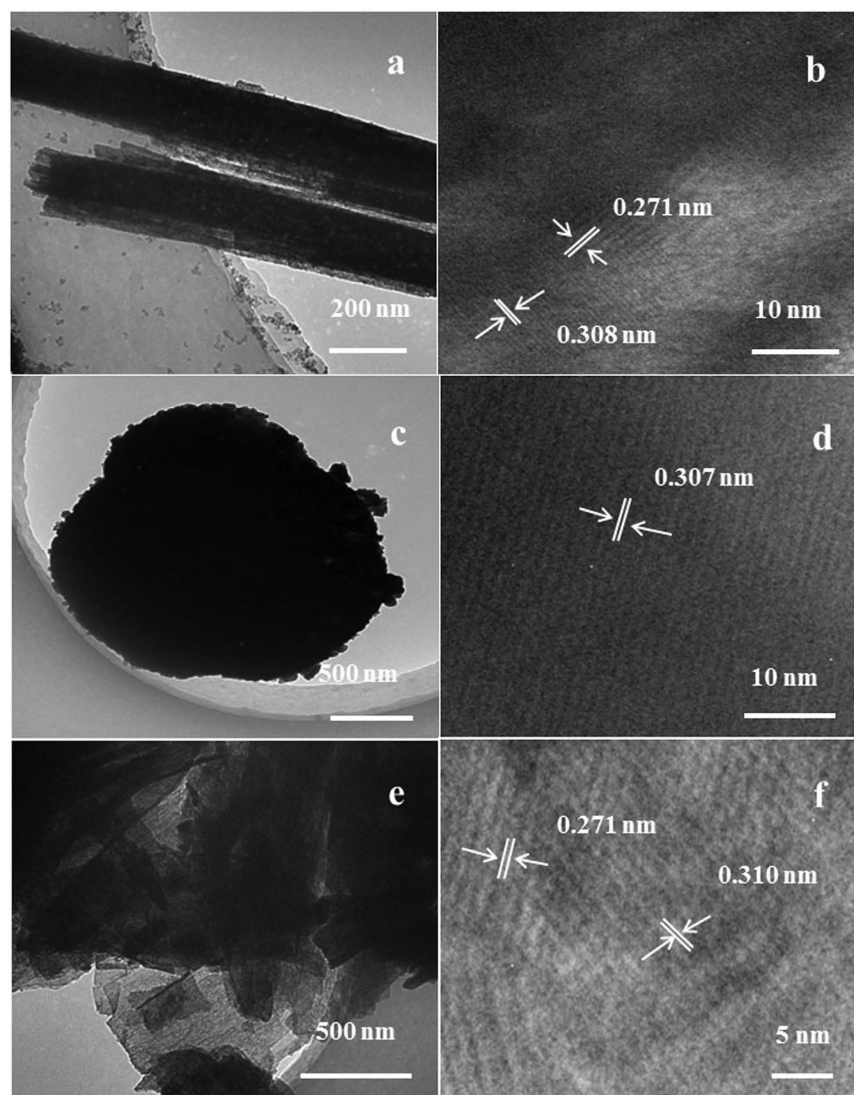
Results

Textural properties. The morphologies of as-prepared CeO_2 with different preparation methods were investigated by the SEM shown in Fig. 1. The morphologies of the CeO_2 catalysts exhibit an outstanding reliance on the preparation methods. SEM images display three different morphologies of CeO_2: nanorods (Ce-R), nanoparticle (Ce-P) and flakes (Ce-F). They were successfully prepared by hydrothermal method and solvothermal method. Figure 1a shows the nanorods with a hierarchical structure consist of many small bars with various thicknesses and lengths. The small bars have uniform diameters of 20–35 nm and form a rod with width of 250 nm and with length of about 2 μm. So much lengths of nanorods were even longer than that of others reported in literatures (300–350 nm)[37,39]. For the Ce-P, the small nanoparticles are about 30–40 nm in diameter and tightly together to form a spherical shape exhibited in Fig. 1b. Figure 1c displays the flower consists of flakes for the Ce-F and the flakes with each petal thickness are approximate 25 nm.

Figure 2 reports the XRD patterns of the Ce-R, Ce-P and Ce-F samples. Their patterns are very similar and the diffraction peaks located at 28.4, 32.8, 47.4, 56.3, 58.8, 69.3, 76.5 and 79.3° that can be assigned to the ceria fluorite structure of the (111), (200), (220), (311), (222), (400), (331) and (420) crystalline faces (JCPDS 65-5923), respectively. Compared to the Ce-P and Ce-F samples, the diffraction peaks of the Ce-R shifted to a low *2θ* angle, indicating the increase in lattice parameters. Rietveld refinements analysis of the XRD profile was carried out (Fig. S1). The lattice parameter was calculated and the obtained results were presented in Table 1. The calculated lattice parameter is approximately 5.4375, 5.4164 and 5.4227 Å for Ce-R, Ce-P and Ce-F, respectively, which are bigger than that of reported for conventional ceria (5.4110 Å)[37], suggesting the lattice expansion for Ce-R, Ce-P and Ce-F. This is most likely due to the existence of more Ce^{3+} in the crystal lattice because the radius of Ce^{3+}

| Catalyst	Lattice parameter (Å)	S_{BET} (m²·g⁻¹)	T_1^a (°C)	T_2^b (°C)	H_{T1}^c (mmol·g$_{cat}$⁻¹)	H_{T2}^d (mmol·g$_{cat}$⁻¹)	$O_{\alpha 1}/O_{\beta}^e$	Ce^{3+f} (%·atom)
Ce-R	5.4375	80	483	798	0.72	0.45	0.87	25.1
Ce-P	5.4113	88	483	745	0.48	0.43	0.74	16.5
Ce-F	5.4164	62	497	768	0.61	0.39	0.77	19.1

Table 1. physicochemical property of Ce-R, Ce-P and Ce-F. [a]The top temperature of the low-temperature peak. [b]The top temperature of the high-temperature peak. [c]The hydrogen consumption at 300–600 °C. [d]The hydrogen consumption at 700–900 °C. [e]From O 1s of XPS analysis. [f]From Ce 3d of XPS analysis.

Figure 3. TEM images of (**a,b**) Ce-R, (**c,d**) Ce-P and (**e,f**) Ce-F.

cations (1.14 Å) is larger than that of Ce^{4+} (0.97 Å) inducing to the lattice expansion[41–43]. According to the XRD results, Ce-R with nanorod structure may possess more defective structures among these CeO_2 samples due to the existence of more Ce^{3+} amounts.

Furthermore, these typical samples were also carefully studied by TEM. The TEM and HRTEM images of the Ce-R sample are reported in Fig. 3a,b. It can be clearly seen that a separate rod composed by small bars from TEM image of Ce-R (Fig. 3a), whereas the HRTEM image (Fig. 3b) shows the clear lattice fringes with inter-planar spacing of 0.308 and 0.271 nm which are assigned to the (111) and (100) crystal planes of CeO_2, respectively[36,37,44]. In Fig. 3c, Ce-P shows a spherical nano-structure, which is accumulated by amount of small nanoparticles. The diameter of spherical particles is about 2 μm, which is consistent with the SEM results (Fig. 1b). After carefully calculation, it is deduced that the dominant lattice fringes spacing of 0.307 nm correspond to the (111) crystal
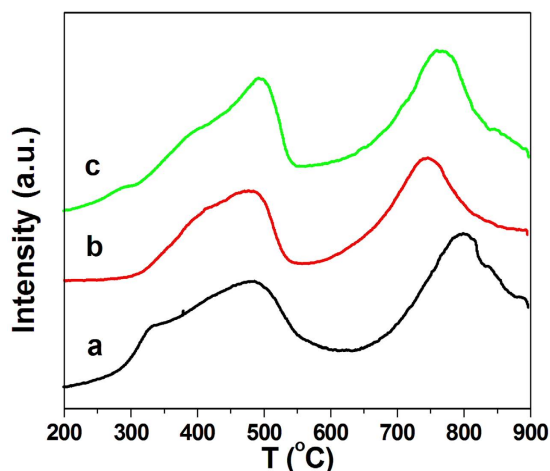
**Figure 4.** H$_2$-TPR curves of (**a**) Ce-R, (**b**) Ce-P and (**c**) Ce-F.

planes of CeO$_2$[36,37] judging from the representative HRTEM image in Fig. 3d. In the TEM image of the Ce-F sample (Fig. 3e), it is clearly observed that the Ce-F possesses flaky structures. The lattice fringes spacing is also calculated to 0.271 and 0.310 nm in the Fig. 3f, which should be recognized as the (100) and (111) crystal plane of CeO$_2$, respectively[36,37,44]., In addition, other region of TEM images for Ce-R and Ce-F are shown in Fig. S2. Combined with XRD results, it confirmed the polycrystalline structure for these CeO$_2$ samples. The three kinds of samples are not optimal oriented growth along with a crystal plane to form single crystalline. The differences in morphologies of as-prepared CeO$_2$ are due to nanoparticles accumulation in a different way with different preparation methods.

H$_2$-TPR characterization.　　The reducibility of Ce-R, Ce-P and Ce-F was studied by H$_2$-TPR shown in Fig. 4. The H$_2$-TPR results of all samples exhibit a bimodal shape with a wide low temperature peak (T$_1$) at 300–600 °C and a wide high temperature peak (T$_2$) at 700–900 °C, which is attributed to the characteristic reduction of surface oxygen and bulk oxygen reduction, respectively[38,39,45]. Overall reduction degree, the hydrogen consumption was calculated at different temperature range by integrating H$_2$-TPR profiles listed in Table 1. The H$_2$ uptake for the low-temperature reduction peak increases with the order of Ce-R (0.72 mmol·g$_{cat}^{-1}$) > Ce-F (0.61 mmol·g$_{cat}^{-1}$) > Ce-P (0.48 mmol·g$_{cat}^{-1}$). It can be seen that the Ce-R possess the largest amount of surface oxygen species among these samples. There is a difference between the top temperatures of the prepared ceria, however, the high-temperature peak is broad and the hydrogen consumption has relatively small deviations in range of 0.39–0.45 mmol·g$_{cat}^{-1}$. Therefore, the prepared CeO$_2$ sample exhibits similar reactivity of lattice oxygen.

In addition, O$_2$-TPD measurements were carried out and the results are shown in Fig. S3. For all the prepared ceria samples, a large and wide peak at the temperature range of 100–600 °C was observed, which was assigned to a continuous desorption of the surface oxygen. The area of peaks by integrating the O$_2$-TPD profiles was 1159, 805 and 774 for Ce-R, Ce-P and Ce-F, respectively, indicating that there is more surface oxygen species on the surface of Ce-R.

XPS characterization.　　XPS was used to investigate the surface chemical properties of all ceria samples in terms of oxidation states and species of surface atoms. The O1s spectra are shown in Fig. 5A, together with their deconvolution obtained by fitting Gaussian peaks after Shirley-background subtraction. The O1s spectra show different features, which depends on both the chemisorbed oxygen species (O$_\alpha$) and lattice oxygen (O$_\beta$). Here, two kinds of surface oxygen species (O$_\alpha$) were identified. The binding energy at 530.5–531.4 eV can be attributed to the defect oxide or the surface oxygen species (O$_{\alpha1}$) adsorbed on the oxygen vacancies (i.e. O$_2^{2-}$, O$^-$, OH$^-$, CO$_3^{2-}$), and the binding energy at 532.7–533.8 eV is assigned to adsorbed oxygen species from hydroxyl species and adsorbed water species (O$_{\alpha2}$) on the surface[46]. The binding energy at 528.8–529.1 eV is ascribed to lattice oxygen (O$_\beta$). In addition, in terms of the quantitation of the surface oxygen species, the ratio of O$_{\alpha1}$ to O$_\beta$ (O$_{\alpha1}$/O$_\beta$) was calculated according to the peak area shown in Table 1. The results present the decrease in the O$_{\alpha1}$/O$_\beta$ value according to the order of Ce-R (0.87) > Ce-F (0.77) > Ce-P (0.74), which is almost consistent with the order of hydrogen consumption at low temperature in H$_2$-TPR (Supplementary Fig. S4). It is confirmed that the surface adsorbed oxygen species of the Ce-R sample is more than that of the others.

Figure 5B shows the XPS spectra in the Ce3d region that was divided into 8 peaks by peak-fitting deconvolution for each sample. The 3d$_{5/2}$ is corresponding to v, while the 3d$_{3/2}$ is corresponding to u. The doublets (v_0, u_0), (v_2, u_2), and (v_3, u_3) represent 3d^{10}4f^0 initial electronic state that are assigned to Ce^{4+}, while the signals (v_1, u_1) represent 3d^{10}4f^1 state of Ce^{3+}[39,47]. Therefore, the relative abundance of the Ce^{3+} (%) species of each sample has been estimated by considering the deconvolution peaks of Ce3d binding energies. In Table 1, Ce^{3+} content is calculated as 25.1%, 19.1% and 16.5% for the Ce-R, Ce-F and Ce-P, respectively. The order follows as: Ce-R > Ce-F > Ce-P, which indicating that the largest Ce^{3+} content (namely 25.1%) on the Ce-R surface among these samples. It is reported that the existence of Ce^{3+} in CeO$_2$ is associate with the formation of oxygen vacancies[39,46]. The larger Ce^{3+} content are observed, the more oxygen vacancies are formed on the surface of the prepared CeO$_2$ samples.
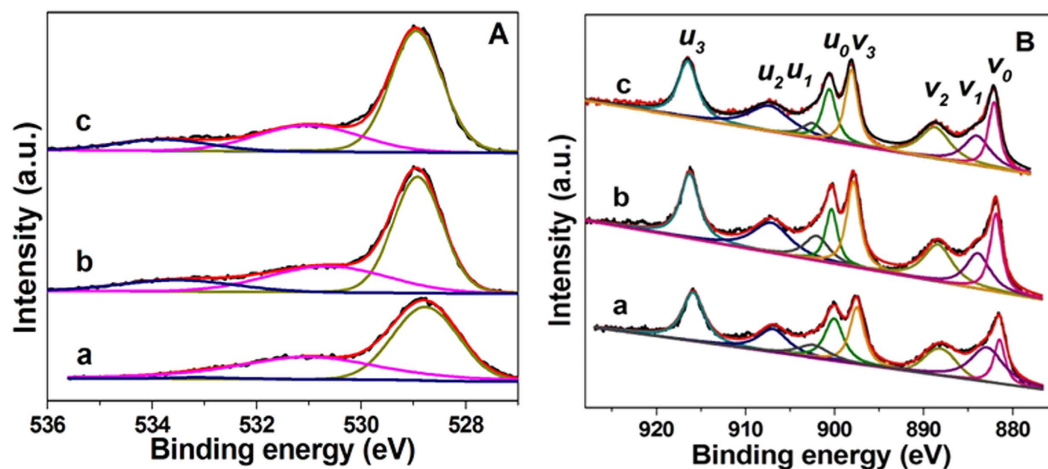
Figure 5. XPS of O 1s (**A**) and Ce 3d (**B**) for (a) Ce-R, (b) Ce-P and (c) Ce-F.

Therefore, the Ce-R sample has the largest Ce^{3+} content on its surface, which implies a relatively higher amount of structure-defects on the surface of the Ce-R. It is favor of formation of surface adsorbed oxygen species. This result is also consisting with the O1s of XPS, H_2-TPR and O_2-TPD results.

In situ DRIFTS characterization. In order to investigate the reactivity of the surface species of the prepared CeO_2 sample, in situ DRIFTS were carried out over these ceria samples under a flow of $0.5vol\%CO/N_2$ and $3vol\%O_2/N_2$ at different temperatures (Fig. 6).

Figure 6a shows in situ DRIFTS of Ce-R. When Ce-R sample adsorbed CO at 30 °C, some characteristic peaks ascribed to the carbonate species appeared at the bands of 1633, 1537, 1519, 1439, 1337, and 1148 cm^{-1}. The bands at 1633 and 1537 cm^{-1} are assigned to bidentate carbonates, while the bands at 1439, 1337 and 1148 cm^{-1} correspond to monodentate carbonates[48–50]. The peak at 1519 cm^{-1} is related to inorganic carboxylate[48–51]. Adding $3vol\%O_2/N_2$ into the feed, the characteristic peaks at 100 °C were in accordance with that of adsorbed CO at 30 °C. When the Ce-R sample was heated from 100 °C to high temperature, the intensities of these peaks began to decrease and gradually disappeared above 300 °C, which suggests that carbonate species on the Ce-R surface occurs to desorption or decomposition.

Figure 6b displays in situ DRIFTS of Ce-P. The IR features observed at the beginning of CO adsorption at 30 °C can be assigned to a mixture of bidentate (1595 and 1284 cm^{-1}), unidentate (1114 and 1044 cm^{-1}) carbonate species[48]. The peak at 1424 cm^{-1} is related to inorganic carboxylate[48–51]. The spectra displayed sensitive changes in intensity as a function of temperature. After the addition of $3vol\%O_2/N_2$ at 50 °C, the spectra appeared to be very similar to the CO adsorption at 30 °C. With increasing the temperature from 150 °C to 250 °C, the sharp peak at 1595 cm^{-1} became stronger and stronger. At temperature of 250 °C and above, new carbonate-type species at 1548 and 1356 cm^{-1} were observed, which were assigned to bidentate carbonates and monodentate carbonates, respectively[48]. It may be CO reacted with lattice oxygen of ceria even in the presence of gaseous O_2 to form new carbonates[52]. When the temperature got to 400 °C, there were also some residual carbonates-like species on the surface of Ce-P, indicating the species were not easy to desorb or decompose.

Figure 6c shows DRIFTS of the Ce-F sample. It appeared similar peaks and evolution of the carbonate species to the Ce-P sample with the reaction temperature. After adding into $3vol\%O_2/N_2$ at 50 °C, the characteristic peaks were in the same with that of adsorbed CO at 30 °C, however, the former was stronger than the latter. The weak peaks assigned to monodentate carbonates at 1114 and 1048 cm^{-1} and inorganic carboxylate at 1427 cm^{-1} became vanish at 150 °C. Specifically, gradual redshift of these peaks was observed with the increase in the temperature and following bands ascribed to bidentate carbonates at 1643–1587 and 1587–1543 cm^{-1}, at the same time, the monodentate carbonates band at 1276 cm^{-1} almost removed to high wavenumber a little and can be observed two new bands at 1301 and 1225 cm^{-1}. It may be carbonates decomposition and CO interacting with surface oxygen/ lattice oxygen form new carbonates simultaneously with the reaction of temperature[52]. With further increasing the temperature, the peaks intensities of carbonate species increase and the residual carbonate species on the surface of Ce-F catalyst also can be seen.

In the DRIFTS (Fig. 6), it observed that carbonates were identified on the samples, but not bicarbonates, although a little hydroxyl content exist the samples surface was suggested in the XPS. It may be the hydroxyl were purge away when the pretreated with N_2 stream.

Soot oxidation activity. Soot combustion reaction is a typical heterogeneous catalytic reaction containing solid particle as reactant. The catalytic activity is related to the temperature at which 10%, 50% and 90% of weight loss is observed (denoted as T_{10}, T_{50} and T_{90}, respectively). The weight-loss curves showing the decomposition profile of the soot mixed with the Ce-R, Ce-P and Ce-F under the loose contact and tight contact are shown in Fig. 7A,B, respectively. The T_{10}, T_{50} and T_{90} values of the catalysts are reported in Table 2. The T_{10}, T_{50} and T_{90} values of Ce-R catalyst are 356, 500 and 554 °C, which are lower than that of Ce-P and Ce-F (Table 2 and Fig. 7A),
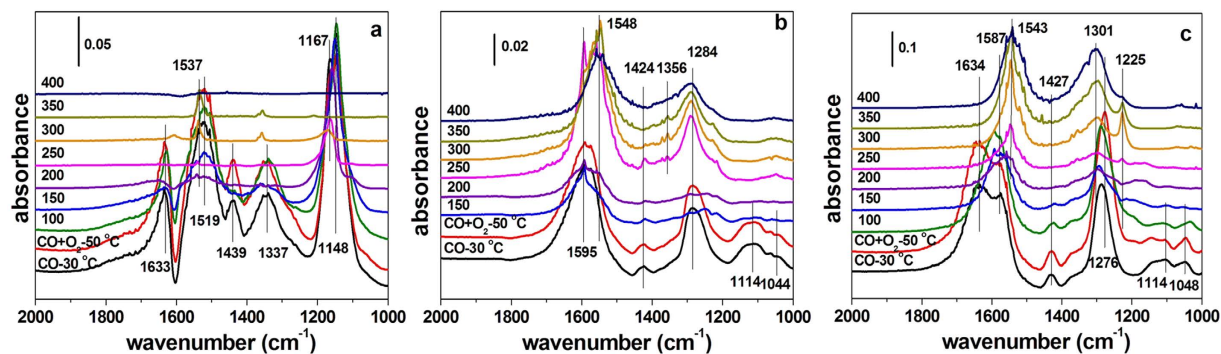
Figure 6. *In situ* DRIFTS of (**a**) Ce-R, (**b**) Ce-P and (**c**) Ce-F (a flow of 0.5vol%CO/N_2 before and after the addition of 3% O_2/N_2 at different temperature).
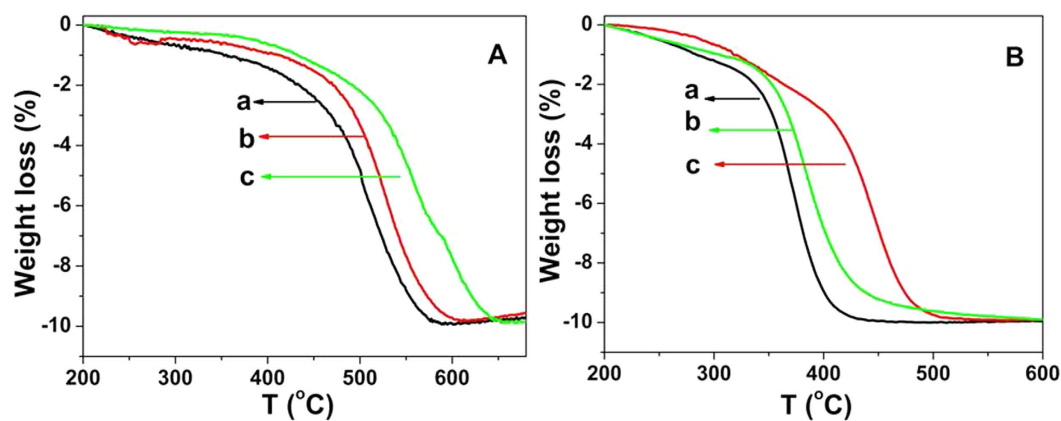
Figure 7. Weight-loss profiles of soot over (a) Ce-R, (b) Ce-P and (c) Ce-F (**A**) under loose contact and (**B**) tight contact in 10vol%O_2/N_2.

Catalyst	Contact condition	T_{10}/ºC	T_{50}/ºC	T_{90}/ºC
Ce-R	Loose	356	500	554
	Tight	286	368	400
Ce-P	Loose	413	521	573
	Tight	320	433	474
Ce-F	Loose	433	554	622
	Tight	306	383	440

Table 2. Catalytic performances of Ce-R, Ce-P and Ce-F in 10vol%O_2/N_2.

indicating Ce-R exhibits much higher activity for soot combustion under loose contact condition. The catalytic activity improves under loose contact condition with the order of Ce-R > Ce-P > Ce-F.

Generally, the mechanical force generates a particularly close contact between the soot and the catalyst in tight contact. Figure 7B illustrates the weight-loss profiles of soot combustion under the tight contact between soot and catalyst. The Ce-R catalyst exhibits the highest catalytic activity for soot oxidation among these catalysts, in which the lowest T_{10}, T_{50} and T_{90} are 286, 368 and 400 °C, respectively (Table 2). Additionally, the catalytic performances of Ce-R were compared with some CeO_2 catalysts that reported in the literatures[37,38,40,53] which are listed in Supplementary Table S1. In our work, the T_m (temperature at the maximal soot combustion rate) values are 372, 439 and 383 °C for Ce-R, Ce-P and Ce-F, respectively. It is found that the T_m values in the literatures are above 400 °C, especially, the T_m values of CeO_2 with nanorod structure reported by Trovarelli *et al.* is 405 °C[38], but it is 368 °C for the Ce-R catalyst. It is clearly seen that the Ce-R possesses an obvious advantage with a much lower T_m value evaluated under the tight contact conditions.

Diesel exhaust contains generally both soot and NO_x as two major pollutants. Thus, the soot combustion with the addition of NO_x was also tested under the tight contact over the above three catalysts. The results of NO oxidation are shown in Fig. 8A and Table 3. The temperature at which the maximal NO_2 concentration attained in the
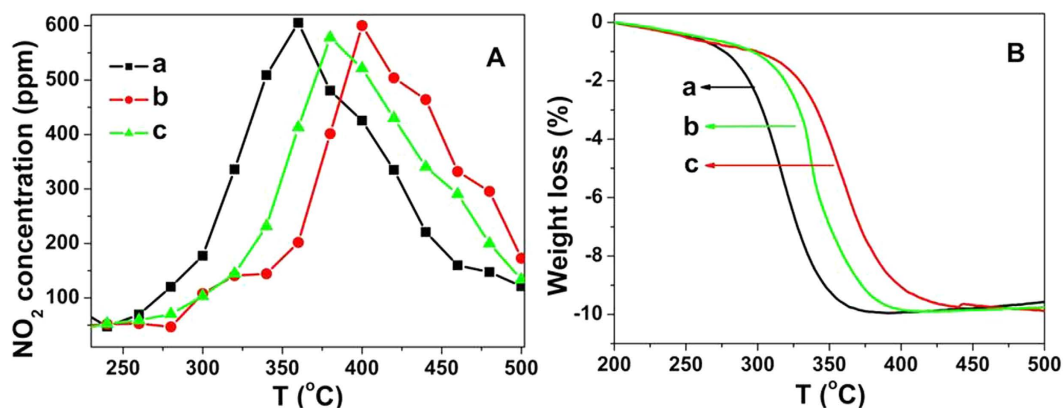
Figure 8. Evolutions of NO_2 concentration (**A**) and the TGA profile (**B**) for (a) Ce-R, (b) Ce-P and (c) Ce-F mixed with soot under the tight contact condition in 1000 ppm NO and 10vol%O_2/N_2.

Catalyst	$T_m(NO_2)$/°C	T_{10}/°C	T_{50}/°C	T_{90}/°C
Ce-R	360	275	315	347
Ce-P	399	301	357	398
Ce-F	379	296	337	372

Table 3. Catalytic performances of Ce-R, Ce-P and Ce-F in 1000 ppm NO and 10vol%O_2/N_2 under tight contact conditions.

outlet gas was denoted as $T_m(NO_2)$. The $T_m(NO_2)$ of Ce-R, Ce-P and Ce-F are 360, 399 and 379 °C, respectively. These results indicate the NO oxidation is remarkable over the Ce-R catalyst.

The weight-loss curves of soot mixed with CeO_2 catalysts with the different morphologies are shown in Fig. 8B and Table 3 under tight contact condition in the presence of NO and O_2. The T_{10} of Ce-R, Ce-P and Ce-F are 275, 301 and 296 °C, respectively. The weight losses of soot combustion for the three catalysts in the presence of NO follow the same order of in the absence of NO. But the soot combustion activities are superior to that in absence of NO conditions. Compared Fig. 8A with Fig. 8B, NO_2 concentration reaches the maximum value when the soot is burned completely. Because NO_2 is a more powerful oxidant than O_2 for soot oxidation[18,19], leading to the NO conversion to NO_2 efficiently decrease the soot combustion temperature. It implies the consumption of NO_2 by reaction with soot at low temperatures which form the surface oxygenated species C(O). Afterwards, the C(O) can either be decomposed to release CO or be oxidized by O_2 to produce CO_2. When the soot reaction is finished, the main production is NO_2.

The above results suggest that the prepared ceria with different morphology exhibits different activity for soot combustion under either loose or tight contact condition. The CeO_2 nanorods exhibit excellent catalytic activity for soot combustion.

Discussion

For catalytic soot oxidation, some authors attribute a key role to the surface/textural properties of ceria[39,42,43], and others agree in explaining the activity of cerium oxide with its oxygen storage and redox capacity[2,38,54,55]. One of the most important roles of CeO_2 in catalytic redox reaction is to provide surface active sites and to act as an oxygen buffer providing oxygen storage/transport by shifting between Ce^{4+} and Ce^{3+} during reaction. In addition, many researchers reported that the contact conditions between the catalyst and soot particles also affect the catalytic performance of soot oxidation[25,38,53].

In this work, we have successfully prepared three different morphologies ceria catalysts (nanorods, nanoparticles and flakes). The soot combustion has been carried out under tight and loose contact conditions between soot and catalyst. The experiment results show that catalytic performance of soot oxidation in tight contact condition is superior to that in loose contact. It is consistent with the results reported by many researchers[38–40,53]. The catalytic activities of as-prepared ceria are much better than that of most of ceria reported in the literatures[37,38,40,53]. We suggest that their redox capacity, the amount of surface oxygen species and the surface area etc. have positively correlated relations with soot oxidation activity according to the above characterizations. From H_2-TPR results (Fig. 4), the reducibility at a low temperature range of the catalysts is well associate with the catalytic activity. The Ce-R sample has the best catalytic activity with the largest hydrogen consumption at low temperature. As shown in Supplementary Fig. S5A,B, there is a positive linear relationship between soot oxidation activities (T_{10}, T_{50} and T_{90}) and the hydrogen consumption of low temperature reduced peak in H_2-TPR (Fig. 4) under either tight contact or loose contact condition. It is noteworthy that the soot conversion temperatures (T_{10}, T_{50} and T_{90}) in the presence of NO (Table 3) also present a good linear function with the hydrogen consumption (Supplementary Fig. S6). As the above results, the reduced peak at low temperature is assigned to the reduction of the surface oxygen species on the prepared ceria samples. The more surface oxygen can improve effectively the catalytic activity

and it may be an important factor for soot oxidation. XPS results also confirm the above opinions, in which there is also a good linear correction between the surface adsorbed oxygen species and the soot combustion activities of T_{10}, T_{50} and T_{90} (Supplementary Fig. S7A,B) under either tight contact or loose contact condition. Thus, the Ce-R sample possesses the maximal amount of surface adsorbed oxygen from H_2-TPR and XPS results, which leads to its best catalytic activity among these prepared ceria samples. It is really confirmed that the possibility for soot oxidation is related to the surface adsorbed oxygen. Some authors considered that the mobility of lattice oxygen may be a key factor on the soot combustion[46]. However, our results did not show a significant difference in the lattice oxygen mobility of as-prepared ceria. Therefore, in our opinions, the number of surface adsorbed oxygen should play a major role in different activity of soot oxidation over the prepared nanostructure ceria catalysts.

In addition, *in situ* DRIFS results prove that the oxidation capacity of the different nano-structure of ceria by the formation and desorption/decomposition of the surface carbonates species. Carbonate species can decompose completely above 300 °C on the surface of Ce-R. But there are the residual carbonates-like species on the surfaces of Ce-P and Ce-F. In general, the degree of surface carbonate species decomposition is associated with the redox of ceria[52]. The carbonate species on the Ce-R surface occurs to desorption or decomposition at a lower temperature. It means CO_2 adsorption on the surface of the Ce-R catalyst is weaker than the Ce-P and Ce-F catalysts. Thus, carbonates species is desorbed easily from the Ce-R catalyst surface and exposes a lot of active sites. It is contribute to the cycle of active sites on the catalyst surface. It indicates that the Ce-R surface exist the higher number of surface adsorbed oxygen than the other samples, which is agreement with the results of H_2-TPR and XPS. Thus, it is further verified that the oxygen species adsorbed on the catalyst surface play crucial role in soot oxidation.

It is noticed that Ce-P exhibits higher activity than the Ce-F for soot combustion in loose contact condition (Table 2 and Fig. 7A); however, the H_2 consumption of Ce-P is slightly less than that of Ce-F. It indicates that other properties such as surface area may also play an important role in loose contact besides surface adsorbed oxygen. It is found that Ce-P and Ce-R possess a relatively larger S_{BET}, which is in the range of 80–88 m²/g. As for Ce-F (62 m²/g), the surface area is lower than that of the Ce-P and Ce-R catalysts. These results indicate that the high surface area can improve the number of contact points between soot and catalyst[6], and then enhance the activity in the loose contact. Bueno-López *et al.* also observed an improved activity with the increase in the surface area over CeO_2 catalyst[54]. Thus, BET surface area may play a role in terms of soot oxidation under the loose contact condition[37].

In summary, Ce-R sample exhibits the best catalytic activity due to the maximal amount of adsorbed oxygen species on its surface.

Conclusions

Ceria catalysts with different morphologies including nanorod, nanoparticle and flake have been successfully prepared and their catalytic behaviors were evaluated for soot combustion. CeO_2 with different morphologies exhibit different physicochemical properties that influence further their catalytic activity of soot combustion. The nanorod CeO_2 with width of 250 nm and length of about 2 μm exhibited the excellent catalytic activity for soot combustion under loose and tight contact conditions in presence/absence of NO. Its activity is higher than that of some CeO_2 catalysts that reported in the literatures, and even reached a level of a precious metal catalyst. The characterization results prove that the difference in catalytic activities is attributed to their surface physicochemical properties derived from different morphologies of CeO_2, in which the adsorbed oxygen species on the surface should be significant factors in soot combustion. In addition, high BET surface area may also be a positive effect on soot oxidation activity under the loose contact conditions.

Methods

Catalysts preparation. CeO_2-nanorod (denoted as Ce-R) has been synthesized through hydrothermal procedure. A typical synthetic procedure is as follow: 0.96 g citric acid and 0.82 g ceria nitrate ($Ce(NO_3)_3 \cdot 6H_2O$) were respectively dissolved in 20 and 10 mL distilled water with vigorous magnetic stirring at room temperature. After ten minutes, 1.20 g urea was added into the citric acid solution. Then the ceria nitrate aqueous solution was gradually dropped into the above mixture, and the mixture was stirred for 30 min. The final mixture was transferred to a Teflon-lined autoclave (40 mL) and heated at 120 °C for 24 h. After cooling to room temperature naturally, the fresh precipitates were collected by centrifugation, washed several times with deionized water and ethanol, respectively, and then dried at 80 °C overnight. Ce-R was obtained by calcination of the as-prepared precursor in air at 500 °C for 4 h.

CeO_2-nanoparticle and CeO_2-nanoflake (denoted hereafter as Ce-P and Ce-F, respectively) have been synthesized through solvothermal method. Briefly, 1.00 g of $Ce(NO_3)_3 \cdot 6H_2O$ was dissolved in 30 mL ethanol with vigorous magnetic stirring at room temperature. 1.00 g (to form nanoparticle)/0.50 g (to form nanoflakes) oxalic acid were added into the solution stirred until dissolved, respectively. The mixture was transferred to a Teflon-lined autoclave (40 mL) and heated at 160 °C for 24 h (to form nanoparticle)/12 h (to form nanoflakes). The precipitates were centrifuged and washed with distilled water and ethanol for several times, and dried at 80 °C overnight to obtain the precursor material. Ce-P and Ce-F samples were obtained by calcining the precursors at 500 °C for 4 h.

Catalysts Characterizations.   The power X-ray diffraction (XRD) analysis were measured on a Rigaku D/max-III B diffractometer with a Cu Kα radiation ($\lambda = 0.15418$ nm), and a working power was 40 kV and 20 mA. SEM images were acquired by using a Hitachi S-4800 microscope at 20 kV. The TEM studies were performed by using a JEM-2010 (JEOL) instrument working with an acceleration voltage of 200 kV. Specific surface area (S_{BET}) was measured according to the BET method by nitrogen adsorption at −196 °C using a Tristar 3020 gas adsorption analyzer (Micromeritics). H_2 temperature-programmed reduction (H_2-TPR) tests were performed by using TP-5080 equipment. 0.020 g catalyst was pre-treated under 5vol%O_2/N_2 stream at 200 °C for 1 h, and then cooled down to room temperature (RT) in the same atmosphere. After purging the sample with 10vol%O_2/N_2 for 30 min, the sample was heated to 900 °C at a rate of 10 °C·min⁻¹ in 5vol%H_2/N_2 (20 mL·min⁻¹). H_2 consumption was recorded using a thermal conductivity detector (TCD), which calibrated with the reduction of known amounts

of CuO. X-ray photoelectron spectroscopy (XPS) was recorded using a Kratos-AXIS ULTRA DLD instrument. *In situ* diffuse reflectance Fourier transform IR (DRIFTS) analysis was recorded with a Nicolet 6700 spectrometer. The high temperature diffuse reflectance IR cell was fitted with ZnSe windows. The spectrum resolution was $4\,cm^{-1}$ in the range of $2000–1000\,cm^{-1}$ and 32 scans were collected. Prior to experiment, the sample was pretreated at room temperature for 1 h in a N_2 stream. Background spectra before CO adsorption were collected in a $40\,mL\cdot min^{-1}$ of N_2 for 30 min. The sample was exposed in a flowing of $0.5vol\%CO/N_2$ $(20\,mL\cdot min^{-1})$ until the saturation of the adsorption at room temperature, and then ramped up from 30 to 450 °C in the $0.5vol\%CO/N_2$ $(20\,mL\cdot min^{-1})$ and $3vol\%O_2/N_2$ $(20\,mL\cdot min^{-1})$ mixture streams.

Catalytic activity measurement. The catalytic activities for soot combustion were evaluated by TG/DTA apparatus (HCP-1 HENVEN Beijing) and measuring the weight loss of catalyst/soot mixtures with the temperature change under different atmospheres: $10vol\%O_2/N_2$ and 1000 ppm NO (when used). Printex-U (Degussa) was used as a model soot. Approximately 9 mg of catalyst were mixed with 1 mg of soot (9:1 on a mass basis), two types of contact conditions were considered, "Loose" contact: the catalyst-soot mixture was prepared by a spatula to homogenize the mixture in a mortar. "Tight" contact: the catalyst-soot mixture was obtained through a pestle to grind soot and catalyst in mortar to reach a close contact. Then, the sample was placed in the sample chamber from 100 to 900 °C at a heating rate of $10\,°C\cdot min^{-1}$ under $10vol\%O_2/N_2$, 1000 ppm NO (when used) with a flow rate of $80\,mL\cdot min^{-1}$ was passed through the reactor. In this work, Temperatures corresponding to 10%, 50% and 90% of weight loss from the TG profile (denoted as T_{10}, T_{50} and T_{90}, respectively) were taken as indices of the activity for each catalyst. The temperature at which the maximal exothermal value attained in the DTA curve according to the maximal soot combustion rate was denoted as T_m. The NO_2 concentration was measured by chemiluminescence NO/NO_X Analyzer (CLD 60) provided by ECO Physics AG (Switzerland). The temperature at which the maximal NO_2 concentration attained in the outlet gas was denoted as $T_m(NO_2)$.

References

1. Bueno-López, A. Diesel soot combustion ceria catalysts. *Appl. Catal. B* **146,** 1–11 (2014).
2. Bueno-López, A., Krishna, K., Makkee, M. & Moulijn, J. A. Active oxygen from CeO_2 and its role in catalysed soot oxidation. *Catal. Lett.* **99,** 203–205 (2005).
3. Oi-Uchisawa, J., Wang, S., Nanba, T., Ohi, A. & Obuchi, A. Improvement of Pt catalyst for soot oxidation using mixed oxide as a support. *Appl. Catal. B* **44,** 207–215 (2003).
4. Wei, Y. C. *et al.* The novel catalysts of truncated polyhedron Pt nanoparticles supported on three-dimensionally ordered macroporous oxides (Mn, Fe, Co, Ni, Cu) with nanoporous walls for soot combustion. *Appl. Catal. B* **146,** 57–70 (2014).
5. Nascimento, L. F., Martins, R. F., Silva, R. F., Sousa Filho, P. C. & Serra, O. A. Ru-doped ceria–zirconia mixed oxides catalyze soot combustion. *Reac Kinet Mech Cat.* **111,** 149–165 (2013).
6. Wei, Y. C., Liu, J., Zhao, Z., Duan, A. J. & Jiang, G. Y. The catalysts of three-dimensionally ordered macroporous $Ce_{1-x}Zr_xO_2$-supported gold nanoparticles for soot combustion: The metal-support interaction. *J. Catal.* **287,** 13–29 (2012).
7. Li, Q. *et al.* A unified intermediate and mechanism for soot combustion on potassium supporteddoxides. *Sci. Rep.* **4,** 4725 (2014).
8. Legutko, P., Jakubek, T., Kaspera, W., Stelmachowski, P., Sojka, Z. & Kotarba, A. Soot oxidation over K-dopedmanganese and iron spinels-How potassium precursor nature and doping level change the catalyst activity. *Catal. Commun.* **43,** 34–37 (2014).
9. López-Suárez, F. E., Bueno-López, A. & Illán-Gómez, M. J. Cu/Al_2O_3 catalysts for soot oxidation: Copper loading effect. *Appl. Catal. B* **84,** 651–658 (2008).
10. Guilhaume, N., Bassou, B., Bergeret, G., Bianchi, D. & Bosselet, F. *In situ* investigation of diesel soot combustion over an $AgMnO_x$ catalyst. *Appl. Catal. B* **119,** 287–296 (2012).
11. Wagloehner, S., Baer, J. N. & Kureti, S. Structure-activity relation of iron oxide catalysts in soot oxidation. *Appl. Catal. B* **147,** 1000–1008 (2014).
12. Hueso, J. L., Caballero, A., Ocana, M. & Gonzalezelipe, A. R. Reactivity of lanthanum substituted cobaltites toward carbon particles. *J. Catal.* **257,** 334–344 (2008).
13. Li, S. X., Reina, Kato, Wang, Q. & Toshiro, Yamanaka. Soot trapping and combustion on nanofibrous perovskite $LaMnO_3$ catalysts under a continuous flow of soot. *Appl. Catal. B* **93,** 383–386 (2010).
14. Guo, X. *et al.* NO_x-assisted soot combustion over dually substituted perovskite catalysts $La_{1-x}K_xCo_{1-y}Pd_yO_{3-\delta}$. *Appl. Catal. B* **142–143,** 278–289 (2013).
15. Yamazaki, K., Kayama, T., Dong, F. & Shinjoh, H. A mechanistic study on soot oxidation over CeO_2-Ag catalyst with 'rice-ball' morphology. *J. Catal.* **282,** 289–298 (2011).
16. Chang, S. J. Shape-dependent interplay between oxygen vacancies and Ag-CeO_2 interaction in Ag/CeO_2 catalysts and their influence on the catalytic activity. *J. Catal.* **293,** 195–204 (2012).
17. Atribak, I., Bueno-López, A. & García-García, A. Thermally stable ceria-zirconia catalysts for soot oxidation by O_2. *Catal. Commun.* **9,** 250–255 (2008).
18. Giménez-Mañogil, J., Bueno-López, A. & García-García, A. Preparation, characterisation and testing of $CuO/Ce_{0.8}Zr_{0.2}O_2$ catalysts for NO oxidation to NO_2 and mild temperature diesel soot combustion. *Appl. Catal. B* **152–153,** 99–107 (2014).
19. Guillén-Hurtado, N., Bueno-López, A. & García-García, A. Catalytic performances of ceria and ceria-zirconia materials for the combustion of diesel soot under NO_x/O_2 and O_2. Importance of the cerium precursor salt. *Appl. Catal. A* **437–438,** 166–172 (2012).
20. Peralta, M. A., Zanuttini, M. S. & Querini, C. A. Activity and stability of $BaKCo/CeO_2$ catalysts for diesel soot oxidation. *Appl. Catal. B* **110,** 90–98 (2011).
21. Zhang, G. Z. *et al.* Three dimensionally ordered macroporous $Ce_{1-x}Zr_xO_2$ solid solutions for diesel soot combustion. *Chem. Commun.* **46,** 457–459 (2010).
22. Liu, J. *et al.* The highly active catalysts of nanometric CeO_2-supported cobalt oxides for soot combustion. *Appl. Catal. B* **84,** 185–195 (2008).
23. Zhang, G. Z. *et al.* Comparative study on the preparation, characterization and catalytic performances of 3DOM Ce-based materials for the combustion of diesel soot. *Appl. Catal. B* **107,** 302–315 (2011).
24. Wei, Y. C. *et al.* H. Highly active catalysts of gold nanoparticles supported on three-dimensionally ordered macroporous $LaFeO_3$ for soot oxidation. *Angew. Chem. Int. Ed.* **50,** 2326–2329 (2011).
25. Wei, Y. C. *et al.* Structural and synergistic effects of three-dimensionally ordered macroporous $Ce_{0.8}Zr_{0.2}O_2$-supported Pt nanoparticles on the catalytic performance for soot combustion. *Appl. Catal. A* **453,** 250–261 (2013).
26. Kebin, Zhou, Yang, Z. Q. & Yang, S. Highly reducible CeO_2 nanotubes. *Chem. Mater.* **19,** 1215–1217 (2007).
27. Zhang, D. S., Shi, L. Y. & Gao, R. H. Shape-controlled synthesis and catalytic application of ceria nanomaterials. *Dalton Trans.* **41,** 14455–14475 (2012).

28. Kullgren, J., Hermansson, K. & Broqvist, P. Supercharged low-temperature oxygen storage capacity of ceria at the nanoscale. *J. Phys. Chem.* **4,** 604–608 (2013).
29. Imagawa, H., Suda, A., Yamamura, K. & Sun, S. Monodisperse CeO_2 nanoparticles and their oxygen storage and release properties. *J. Phys. Chem. C* **115,** 1740–1745 (2011).
30. Umar, A., Kumar, R., Akhtar, M. S., Kumar, G. & Kim, S. H. Growth and properties of well-crystalline cerium oxide (CeO_2) nanoflakes for environmental and sensor applications. *J. Colloid Interf Sci.* **454,** 61–68 (2015).
31. Tong, X. F. *et al.* Shape-dependent activity of ceria for hydrogen electro-oxidation in reduced-temperature solid oxide fuel cells. *Small.* **11,** 5581–5588 (2015).
32. Zhou, K. B., Wang, X., Sun, X. M., Peng, Q. & Li, Y. D. Enhanced catalytic activity of ceria nanorods from well-defined reactive crystal planes. *J. Catal.* **229,** 206–212 (2005).
33. Gao, Y. X. *et al.* Morphology-dependent interplay of reduction behaviors, oxygen vacancies and hydroxyl reactivity of CeO_2 nanocrystals. *Phys. Chem. Chem. Phys.* **17,** 31862–31871 (2015).
34. Mai, H. X. *et al.* Shape-selective synthesis and oxygen storage behavior of ceria nanopolyhedra, nanorods, and nanocubes. *J. Phys. Chem. B* **109,** 24380–24385 (2005).
35. Han, W. Q., Wu, L. J. & Zhu, Y. M. Formation and oxidation state of CeO_{2-x} nanotubes. *J. Am. Chem. Soc.* **127,** 12814–12815 (2005).
36. Tana. *et al.* Morphology-dependent redox and catalytic properties of CeO_2 nanostructures: Nanowires, nanorods and nanoparticles. *Catal. Today.* **148,** 179–183 (2009).
37. Aneggi, E., Wiater, D., Leitenburg, C., Llorca. J. & Trovarelli, A. Shape-dependent activity of ceria in soot combustion. *ACS Catal.* **4,** 172–181 (2014).
38. Miceli, P., Bensaid, S., Russo, N. & Fino, D. CeO_2-based catalysts with engineered morphologies for soot oxidation to enhance soot-catalyst contact. *Nanoscale. Res. Lett.* **9,** 254 (2014).
39. Piumetti, M., Bensaid, S., Russo, N. & Fino, D. Nanostructured ceria-based catalysts for soot combustion: Investigations on the surface sensitivity. *Appl. Catal. B* **165,** 742–751 (2015).
40. Kumar, P. A., Tanwar, M. D., Bensaid, S., Russo, N. & Fino, D. Soot combustion improvement in diesel particulate filters catalyzed with ceria nanofiber. *Chem. Eng. J.* **207–208,** 258–266 (2012).
41. Xu, B., Zhang, Q., Yuan, S., Zhang, M. & Ohno, T. Morphology control and characterization of broom-like porous CeO_2. *Chem. Eng. J.* **260,** 126–132 (2015).
42. Zhou, X. D. & Huebner, W. Size-induced lattice relaxation in CeO_2 nanoparticles. *Appl. Phys. Lett.* **79,** 3512 (2001).
43. Zhang, F. *et al.* Cerium oxide nanoparticles: Size-selective formation and structure analysis. *Appl. Phys. Lett.* **80,** 127 (2002).
44. Si, R. & Flytzani-Stephanopoulos, M. Shape and crystal-plane effects of nanoscale ceria on the activity of Au-CeO_2 catalysts for the water-gas shift reaction. *Angew. Chem. Int. Ed.* **47,** 2884–2887 (2008).
45. Valencia, M. *et al.* Evidences of the cerium oxide-catalysed DPF regeneration in a real diesel engine exhaust. *Top. Catal.* **56,** 452–456 (2013).
46. Shen, Q. *et al.* Facile synthesis of catalytically active CeO_2 for soot combustion. *Catal. Sci. Technol.* **5,** 1941–1952 (2015).
47. Zhang, G. J. Synthesis and characterization of mesoporous ceria with hierarchical nanoarchitecture controlled by amino acids. *J. Phys. Chem. B* **110,** 25782–25790 (2006).
48. Li, C. Carbon monoxide and carbon dioxide adsorption on cerium oxide studied by Fourier- transform infrared spectroscopy. *J. Chem. Soc.* **85,** 929–943 (1989).
49. Bera, P., Cámara, A. L., Hornés, A. & Martínez-Arias, A. Comparative *in situ* DRIFTS-MS study of ^{12}CO- and ^{13}CO-TPR on CuO/CeO_2 catalyst. *J. Phys. Chem. C* **113,** 10689–10695 (2009).
50. Binet, C., Daturi, M. & Lavalley, C. J. IR study of polycrystalline ceria properties in oxidised and reduced states. *Catal. Today.* **50,** 207–225 (1999).
51. Trovarelli, A. Catalytic properties of ceria and CeO_2-containing materials. *Catal. Rev.* **38,** 439–520 (1996).
52. Wu, Z. L., Li, M. J. & Overbury, S. H. On the structure dependence of CO oxidation over CeO_2 nanocrystals with well-defined surface planes. *J. Catal.* **285,** 61–73 (2012).
53. Bensaid, S., Russo, N. & Fino, D. CeO_2 catalysts with fibrous morphology for soot oxidation: The importance of the soot-catalyst contact conditions. *Catal. Today* **216,** 57–63 (2013).
54. Buenolopez, A., Krishna, K., Makkee, M. & Moulijn, J. Enhanced soot oxidation by lattice oxygen via La^{3+}-doped CeO_2. *J. Catal.* **230,** 237–248 (2005).
55. Liang, Q., Wu, X. D., Wu, X. D. & Weng, D. Role of surface area in oxygen storage capacity of ceria-zirconia as soot combustion catalyst. *Catal. Lett.* **119,** 265–270 (2007).

Acknowledgements

Author Contributions

W.Z. performed the experimental works, analyzed results. F.Y., L.C. and X.N. assisted in the analyses of results. Y.Z. proposed, planned, and designed the project and reviewed the manuscript prior to submission. All authors wrote the manuscript.

Additional Information

Supplementary information accompanies this paper at http://www.nature.com/srep

Competing financial interests: The authors declare no competing financial interests.

How to cite this article: Zhang, W. *et al.* Soot Combustion over Nanostructured Ceria with Different Morphologies. *Sci. Rep.* **6,** 29062; doi: 10.1038/srep29062 (2016).